Nano Energy 73 (2020) 104796

Contents lists available at ScienceDirect

Nano Energy

journal homepage: http://www.elsevier.com/locate/nanoen

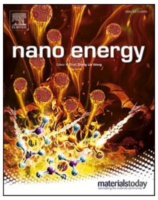

# Electronic and geometric structure engineering of bicontinuous porous Ag–Cu nanoarchitectures for realizing selectivity-tunable electrochemical $CO_2$ reduction

Wenjun Zhang [a,1], Chenhong Xu [a,1], Yi Hu [a], Songyuan Yang [a], Lianbo Ma [a], Lei Wang [a], Peiyang Zhao [a], Caixing Wang [a], Jing Ma [a,**], Zhong Jin [a,b,*]

[a] Key Laboratory of Mesoscopic Chemistry of MOE, Jiangsu Key Laboratory of Advanced Organic Materials, School of Chemistry and Chemical Engineering, Nanjing University, Nanjing, 210023, China

[b] Shenzhen Research Institute of Nanjing University, Shenzhen, 518063, China

## ARTICLE INFO

*Keywords:*
Electrocatalytic $CO_2$ reduction
Ag–Cu bicontinuous porous nanostructures
Tunable product selectivity
Electronic structures
Geometric effects

## ABSTRACT

The electrochemical conversion of waste carbon dioxide into hydrocarbon fuels represent a promising strategy for clean and sustainable energy production. However, the design of outstanding electrocatalysts that can reduce $CO_2$ in an efficient and selective manner is challenging, and the fundamental understanding on reaction mechanism is still limited. Herein, we report the preparation of self-supported Ag–Cu bimetallic catalysts with bicontinuous nanoporous geometries and adjustable compositions through an electrochemical anodizing/dealloying process of $Ag_{52}Cu_{39}Sn_9$ alloy foil to exploit their performances in electrocatalytic $CO_2$ reduction. By changing the compositions from $Ag_{91}Cu_9$ to $Ag_{65}Cu_{35}$, the variations in atomic arrangement and electronic structure around the active sites bring synergistic effects on the binding strength of different reaction intermediates, realizing tunable product selectivity from CO to formate at high Faradaic efficiencies. *In-situ* Raman analysis and density functional theory calculations confirm that as the Ag–Cu atomic ratio shifts, the variations of formation free-energies and desorption capacities of intermediates lead to different reaction pathways and final products. The findings in this study provide a promising route to modulate the atomic structures and improve the properties of electrocatalysts towards $CO_2$ fixation.

## 1. Introduction

Carbon dioxide ($CO_2$) is one of the disturbing greenhouse gases released from the excessive use of fossil fuels [1,2]. Converting $CO_2$ molecules into organic chemicals through artificial photosynthesis is an ideal approach to make our society more sustainable [3]. Through renewable energy utilization [4–6], electrochemical $CO_2$ reduction reaction ($CO_2RR$) has been regarded as a promising approach to produce useful carbonaceous compounds, which can either be directly used as fuels, or be converted into high-value added chemicals through further chemical engineering processing. For example, formate ($HCOO^-$/HCOOH), as a possible product, can be applied as a hydrogen carrier in fuel cells with the merits of easy storage and high safety [7,8]. Another possible product, Carbon monoxide (CO), is an important feedstock to produce olefins through Fischer-Tropsch process [9,10], which could reduce $CO_2$ emission by 40% [11]. However, $CO_2$ as a fully-oxidized and thermodynamically-stable molecule brings great challenges for $CO_2RR$. Especially, the energy barriers for the activation of $CO_2$ molecules and the dissociation of carbon-oxygen bonds are considerably high [12]. To resolve these problems, high-performance electrocatalysts should be explored. Moreover, most existing catalysts focused on improving the $CO_2RR$ selectivity for only one product, the tunable selectivities for different useful products at high levels cannot be easily realized.

Precious metal nanocrystals (Au and Pd, etc.) have been employed as the electrocatalysts in $CO_2$ electroreduction for highly-selective $C_1$ chemicals production [13]. However, these noble metals are not suitable

---

* Corresponding author. Key Laboratory of Mesoscopic Chemistry of MOE, Jiangsu Key Laboratory of Advanced Organic Materials, School of Chemistry and Chemical Engineering, Nanjing University, Nanjing, 210023, China.

** Corresponding author.

*E-mail addresses:* majing@nju.edu.cn (J. Ma), zhongjin@nju.edu.cn (Z. Jin).

[1] These two authors contributed equally to this work.

https://doi.org/10.1016/j.nanoen.2020.104796
Received 30 October 2019; Received in revised form 15 March 2020; Accepted 2 April 2020
Available online 17 April 2020

for large-scale applications owing to their high cost and low abundance. Some inexpensive alternatives, such as Cu, Sn and Bi have also shown promising properties in $CO_2$ conversion in terms of their notoriously poor activity towards competitive hydrogen evolution reaction (HER) [14]. In this regard, metal alloys could be employed as effective alternatives to tune the catalytic activity and selectivity of $CO_2$RR [15–20]. Alloying could bring about electronic effects associated with d-band theory, and/or geometric effects related to the atomic arrangement around the active sites. To be specific, once the electronic density of the reaction center is modulated to an appropriate value matching the energy level of reacting species, electrons could be easily transferred between substrates and products. Meanwhile, the change in the electronic structure of a catalyst also leads to the electronic effects on the binding strength of intermediates. In terms of transition metal alloys, as the compositions are changed, the shifting of the d-band center could determine the interaction behavior of intermediates with the catalysts, thus leading to different reaction pathways. From the viewpoint of the geometric effect, the way the active site is configured can also play an indispensable effect on the binding strength of intermediates. To achieve the attractive properties, developing multi-metallic catalysts could lower the reaction energy barrier and tune the binding behavior of all intermediates to realize high-performance $CO_2$ conversion into different chemical products.

Herein, considering the intrinsic chemical characteristics of the ternary metallic components, we report the preparation of two distinct self-supporting Ag–Cu bimetallic catalysts with different bicontinuous porous structures and compositions: the sponge-like $Ag_{91}Cu_9$ alloy nanostructure (spongeous $Ag_{91}Cu_9$) with 3D nanoporosity and the coral-like $Ag_{65}Cu_{35}$ alloy nanostructure (coralline $Ag_{65}Cu_{35}$) with nanodendritic morphology through a controlled and scalable electrochemical anodizing/dealloying process of $Ag_{52}Cu_{39}Sn_9$ alloy foil (Fig. 1a). These Ag–Cu bimetallic catalysts are applied to $CO_2$ electro-reduction, and the catalytic performances are verified to be closely associated with their unique structures and compositions. The 3D porous morphology and hierarchical dendritic structure provide holes and interior void space [21–23], create large surface area and high degree of connectivity [24, 25], both resulting in large electrochemical surface area (ECSA) and highly-active local sites, thus facilitate $CO_2$ adsorption, electron transfer and adsorbate binding capability. As the compositions shift, the variations in electronic structure and local atomic rearrangement synergistically modulate the interaction strength of reaction intermediates, resulting in tunable main product yields between CO and HCOOH. The

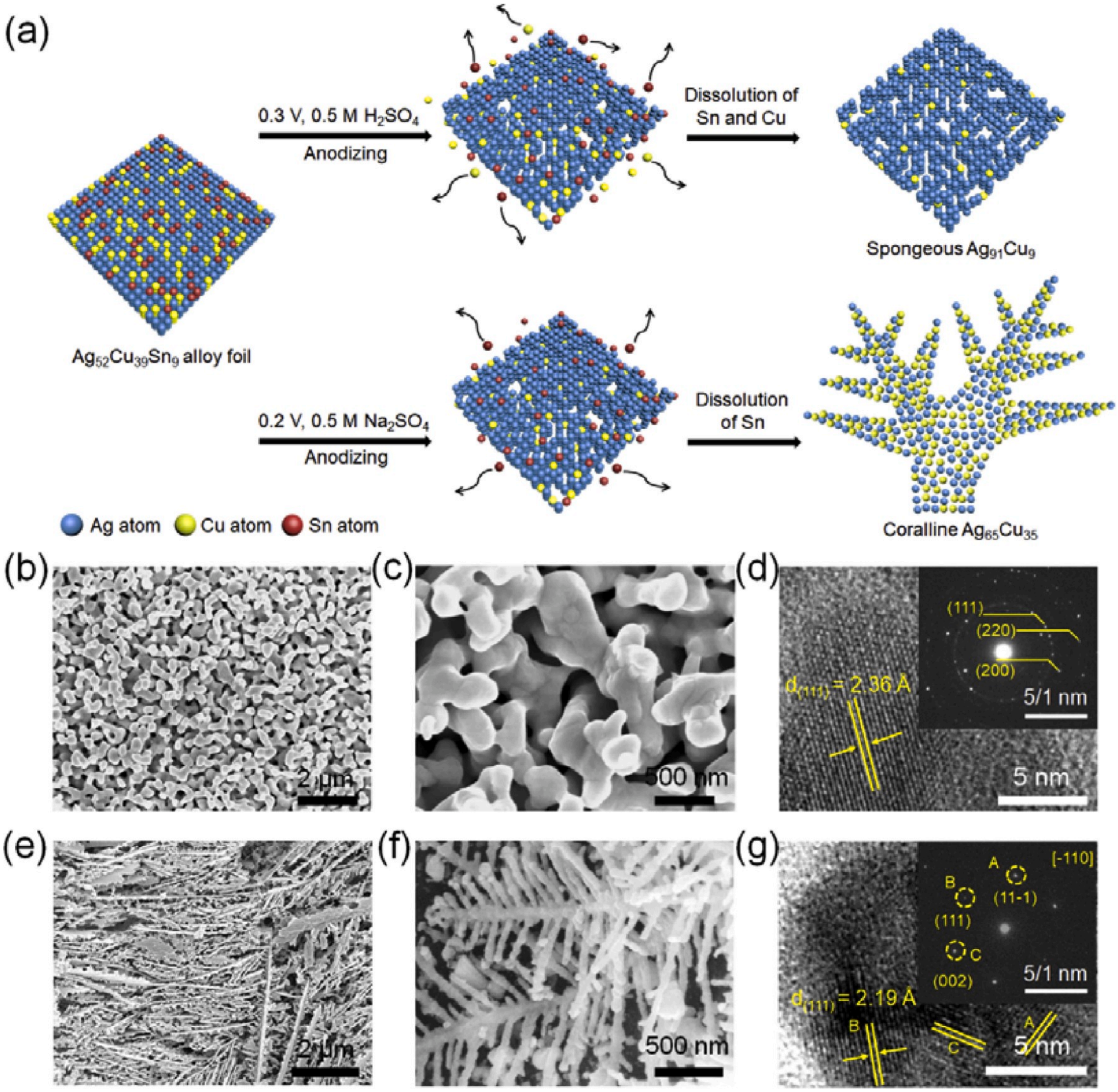

**Fig. 1.** (a) Schematic synthesis route of spongeous $Ag_{91}Cu_9$ and coralline $Ag_{65}Cu_{35}$ *via* an electrochemical anodizing/dealloying process of $Ag_{52}Cu_{39}Sn_9$ alloy foil. (b, c) SEM images of spongeous $Ag_{91}Cu_9$ at different magnifications. (d) HRTEM image of spongeous $Ag_{91}Cu_9$. (e, f) SEM images of coralline $Ag_{65}Cu_{35}$ at different magnifications. (g) HRTEM image of coralline $Ag_{65}Cu_{35}$. The insets in (d, g) are the SAED patterns of spongeous $Ag_{91}Cu_9$ and coralline $Ag_{65}Cu_{35}$, respectively.

as-obtained Ag–Cu electrocatalysts achieve good activity, tunable selectivity and high long-term stability towards $CO_2$RR. Moreover, *in-situ* Raman analysis and density functional theory (DFT) calculations were conducted to further explore the possible reaction pathways which were rationalized by the variations of formation free-energies and desorption capacities of intermediates.

## 2. Experimental section

### 2.1. Chemicals

Commercial bulk Ag, Sn and Cu were purchased from Zhongnuoxincai Technology Co., LTD., Beijing. Sodium bicarbonate ($KHCO_3$), sulfuric acid ($H_2SO_4$), sulfuric sulfate ($Na_2SO_4$), sodium formate ($HCOONa·2H_2O$, 99.99%) and N-methyl pyrrolidone (NMP) were purchased from Sinopharm Chemical Reagent Corp. Dimethylsulfoxide (DMSO, 99.95%) was purchased from Alfa Aesar. Deuteroxide ($D_2O$, 99.9%) were purchased from Sigma Aldrich. All the chemicals in analytical grade were used for experiments without further purification. All the aqueous solutions were prepared with ultrapure water (18.2 mΩ cm, Millipore SAS, France).

### 2.2. Synthesis of $Ag_{52}Sn_{39}Cu_9$ alloy foils

$Ag_{52}Sn_{39}Cu_9$ alloy foils were prepared by melting commercial bulk Ag, Sn and Cu with a certain atomic ratio of 52:39:9 in a high-vacuum arc furnace (DHL-400, Shenyang SKY Technology) at a high current of 220 A for 3 min, and then repeated it five times. Subsequently, the obtained $Ag_{52}Sn_{39}Cu_9$ melt was rapidly cast into ingots in an iron chill mold. Then, the $Ag_{52}Sn_{39}Cu_9$ ingots was re-melted in a quartz crucible by high-frequency induction heating under Ar atmosphere and was melt-spun onto a copper roller at a circumferential speed of about 35 m $s^{-1}$ by using a single roller melt spinning apparatus (SP009A, Beijing Physcience). The obtained $Ag_{52}Sn_{39}Cu_9$ alloy foils were generally 20–30 μm in thickness, 2–5 mm in width, and several centimeters in length.

### 2.3. Synthesis of spongeous $Ag_{91}Cu_9$ and coralline $Ag_{65}Cu_{35}$

The spongeous $Ag_{91}Cu_9$ and coralline $Ag_{65}Cu_{35}$ were prepared from $Ag_{52}Sn_{39}Cu_9$ alloy foil *via* an electrochemical anodizing/etching method. The anodizing process was conducted in a conventional three-electrode system, with a platinum (Pt) electrode and a SCE as counter electrode and reference electrode, respectively. To prepare spongeous $Ag_{91}Cu_9$, $Ag_{52}Sn_{39}Cu_9$ alloy foil as the working electrode was etched in $N_2$-saturated 0.5 M $H_2SO_4$ aqueous solution at an applied potential of 0.3 V (*vs.* SCE) for 3 h. When the etching was completed, no more gas bubbles was produced on the surface of Pt electrode and a steady, near-zero current was measured. Then, the obtained spongeous $Ag_{91}Cu_9$ was carefully rinsed with distilled water and ethanol for several times, followed by drying at 50 °C under vacuum for 24 h. The resulting sample was kept in an Ar-filled glovebox under room temperature to avoid possible oxidation. Coralline $Ag_{65}Cu_{35}$ was prepared in the similar way at an applied potential of 0.2 V (*vs.* SCE) for 40 min, and the $H_2SO_4$ solution etchant was replaced by $Na_2SO_4$ solution.

### 2.4. Synthesis of nanoporous Cu

The nanoporous Cu was prepared from commercial $Cu_{60}Zn_{40}$ alloy foil *via* a similar electrochemical dealloying method. The $Cu_{60}Zn_{40}$ alloy foil (30 μm in thickness) was first washed by alcohol to remove surface contaminations and then used as the working electrode. A Pt electrode and a SCE were used as counter electrode and reference electrode, respectively. Then, $Cu_{60}Zn_{40}$ alloy foil was etched in $N_2$-saturated 0.5 M HCl aqueous solution at an applied potential of 0.4 V (*vs.* SCE) for 70 min until a near-zero current was measured. Then, the as-obtained nanoporous Cu was rinsed with distilled water and ethanol for several times, followed by drying in vacuum at 60 °C for 6 h, and stored in an Ar-filled glovebox prior to use.

### 2.5. Characterizations

The morphology and microstructure of all samples were characterized by a field-emission scanning electron microscope (FESEM, NanoSEM Nova 450, FEI) and transmission electron microscopy (TEM, JEM-2100). Elemental mappings of samples were performed by the energy-dispersive X-ray spectrometry (EDX, Bruker Quantax-100) accessory of the SEM. The crystal structures of samples were analyzed by powder X-ray diffractometer (XRD, Bruker D8 Advance) with Cu Kα (λ = 1.5406 Å) irradiation in the range of 30–90° at a scanning speed of 10° $min^{-1}$. The elemental distributions of catalysts before and after the electrolysis were analyzed by X-ray photoelectron spectroscopy (XPS, PHI-5000 Versa Probe) with an Al *Kα* X-ray radiation. The elemental composition ratios were measured with inductively-coupled plasma-optical emission spectrometer (ICP-OES, Optima 5300DV) by dissolving the as-prepared samples in a high-concentration $HNO_3$ aqueous solution (1:1 in volume).

### 2.6. Electrochemical measurements

All electrochemical measurements were carried out in a conventional three-electrode system with a CHI-760E electrochemical workstation. Liner sweep voltammetry (LSV) measurements were performed in $N_2$- or $CO_2$- saturated 0.1 M $KHCO_3$ electrolyte at a scan rate of 20 mV $min^{-1}$ in the voltage range from 0.0 to −1.2 V (*vs.* RHE). Cyclic voltammetry (CV) was employed to determine the electrochemical surface area (ECSA) of different samples. CV experiments were performed in $N_2$-saturated 0.1 M $KHCO_3$ electrolyte within a potential range from −0.3 V to −0.2 V (*vs.* Ag/AgCl) to ensure the nonoccurrence of Faradaic processes. The scan rates were set to 10, 15, 20, 30, 40 and 50 mV $s^{-1}$, respectively. The ECSA value is in direct proportion to the ratio of double-layer capacitance ($C$dl) of the working electrode. The slope of the linear regression, twice that of $C$dl, is estimated by plotting the capacitive current density ($\Delta J = (J_a\text{-} J_c)$, where $J_a$ and $J_c$ are the cathodic and anodic current densities, respectively) at −0.25 V (*vs.* Ag/AgCl) against the scan rates from the scan-rate dependence of CV curves. The $J_{CO}$ (or $J_{formate}$) was calculated by the geometric current density and Faradaic efficiency of CO (or formate), and the Tafel slop for CO (or formate) was analyzed by the plot of overpotential *vs.* the logarithm of $J_{CO}$ (or $J_{formate}$). Electrochemical $CO_2$RR performances were measured in a H-type commercial electrochemical cell (Ida Technology Co., LTD., Tianjin) at atmospheric pressure and room temperature (25 °C) with a cycle condensing unit. The sealed cell was separated into two compartments with a piece of pre-treated proton exchange membrane (Nafion-117), and each compartment was filled with 30 mL of 0.1 M $KHCO_3$ aqueous solution with gas headspace of approximately 20 mL. After saturated with $CO_2$ gas in both anodic and cathodic compartments for at least 30 min, the pH value of the electrolyte was tested to be ~6.8. The electrolytes in both compartments were continuously stirred at 1000 rpm with stirring bars during $CO_2$ electrolysis. The as-obtained nanostructural metal foils were employed as working electrodes. The geometric electrode area used for electrolysis was about 0.25 $cm^2$. Platinum gauze electrode and Ag/AgCl (saturated KCl) electrode were used as counter electrode and reference electrode, respectively. All the applied potentials are calibrated as reversible hydrogen electrode (RHE) potentials by using the Nernst equation as below.

$$E\ (vs.\ \text{RHE}) = E\ (vs.\ \text{Ag/AgCl}) + 0.1989\ \text{V} + 0.059 \times \text{pH} \tag{1}$$

### 2.7. Quantitative analysis of gaseous and liquid products

During the electrochemical $CO_2$RR process, a small quantity of generated gases (500 μL) was collected from the headspace by a gastight syringe in 30 min intervals and rapidly injected into the gas sampling loop of a gas chromatograph (GC7900, Shanghai Techcomp) to quantify the amount of gas products (n in moles). The different components in the gaseous products were separated and detected by a thermal conductivity detector (for $H_2$) and a flame ionization detector (for CO and hydrocarbons) with high-purity argon (Ar) as a carrier gas. To confirm the accuracy of gas product yields, each quantitative sampling was carried out for two times. The yield of gas products was calculated from the standard curves using different amounts of highly-purified gas mixture containing $H_2$, CO, $CH_4$, $C_2H_4$ and $CO_2$ gases. The linear relationship between the known gas amounts and relative areas was made into a standard curve.

After the electrolysis process, the remained electrolyte was stored to quantificationally analyze the liquid products (n in moles) by nuclear magnetic resonance technique (NMR, Bruker AV-600). Typically, 0.6 mL of electrolyte was uniformly mixed with 0.1 mL of deuterated water ($D_2O$) and 0.1 mL of anhydrous dimethyl sulfoxide (DMSO, 99.5%, diluted to 10 ppm (v/v) by water prior to use) as an internal standard. The one-dimensional $^1$H spectrum was carried out with necessary water peak suppression by a water pre-saturation method. The concentration of formate or ethanol was determined by the standard curve using various concentrations (0.5, 1.0, 2.0, 5.0 and 10 mM) of sodium formate or (0.5, 0.9, 1.0, 1.2, and 1.5 mM) dehydrate ethanol and the internal standard (10 ppm DMSO). The linear relationship between the known formate/ethanol concentrations and relative areas (*vs.* 10 ppm DMSO) was made into a standard curve. The Faradaic efficiency (*FE*) of specific products can be calculated *via* the following equation:

$$\textit{Faradaic Efficiency} = mF \times n/Q = mF \times n/(I \times t) \tag{2}$$

where *F* is the faraday constant, *n* (in mole) is the amount of the specific product and *m* (in number) indicates the required electrons for the generation of the specific molecule (e.g., $H_2$, CO, HCOOH, etc.). The amount of charges (*Q* in coulombs) for producing the product was calculated during a period of reaction time. *I* (in amperes) is the constant current at an applied voltage and *t* (in seconds) is the time consumed at the corresponding current during the electrolysis process.

### 2.8. In-situ Raman analysis

*In-situ* Raman experiments were performed in an *in-situ* spectroelectrochemical cell (Gaossunion Co., LTD., Wuhan) with a confocal Raman microscope (Horiba JY Evolution). A He–Ne laser with 473 nm wavelength was used as the excitation source. The working electrode was spongeous $Ag_{91}Cu_9$ or coralline $Ag_{65}Cu_{35}$ which was attached on a titanium foil. A Pt wire electrode and Ag/AgCl (saturated KCl) electrode were used as counter electrode and reference electrode, respectively. 3 mL of 0.1 M $KHCO_3$ aqueous solution was purged with Ar for 15 min to remove oxygen, and was consequently saturated with $CO_2$ by introducing $CO_2$ gas in the solution for 15 min. *In-situ* Raman measurements were performed at a constant applied potential of −0.7 V (*vs.* RHE) for spongeous $Ag_{91}Cu_9$ with the wavenumber range between 90 and 2200 $cm^{-1}$, and the acquisition time for each Raman spectrum was 50 s. *In-situ* Raman measurements for coralline $Ag_{65}Cu_{35}$ was conducted at the same way as spongeous $Ag_{91}Cu_9$, except the applied potential was held at −1.0 V (*vs.* RHE).

### 2.9. Computational method

All calculations were carried using the pseudo-potential plane-wave DFT (density functional theory), which was implemented in CASTEP. GGA (generalized gradient approximation) with PBE (Perdew-Burke-Ernzerhof) functional was employed as the exchange-correlation functional. The Kohn-Sham wave functions were expanded using plane waves with a cutoff energy of 400 eV. The Broyden-Fletcher-Goldfarb-Shanno optimization method was employed with the setting convergence tolerance of energy of $2.0 \times 10^{-5}$ eV/atom, maximum force of 0.05 eV/Å, and maximum displacement of $2.0 \times 10^{-3}$ Å, respectively. A 12 Å vacuum space along the c-axis was used to eliminate the interactions between repeat cells in periodic boundary condition calculations.

A slab with four atomic layers and 4 × 4 unit cells containing 64 atoms was chosen in our calculations. The $Ag_7Cu_1$ and $Ag_5Cu_3$ slabs were built by replacing 1/8 and 3/8 Ag atoms in the Ag slab with Cu atoms, respectively. The bulk lattice constants of $Ag_8Cu_0$, $Ag_7Cu_1$ and $Ag_5Cu_3$ were optimized using the 8 × 8 × 8 Monkhorst-Pack type of k-point sampling. The calculation of isolated small molecules was performed by using a 10 Å × 10 Å × 10 Å unit cell with the Γ-point only for the k-point sampling. We used the 4 × 4 × 1 Monkhorst-Pack type of k-point sampling of slab calculations. The surface energy ($E_{surf}$) was calculated by using the following equation:

$$E_{surf} = \frac{1}{2A}\left(E_{slab} - NE_{unit}\right) \tag{3}$$

where $E_{slab}$ was the total energy of the selected slab supercell, $E_{unit}$ was the primitive cell energy of the bulk, *N* was the multiple of the atoms for the selected supercell in comparison with those of the primitive cell, *A* was the area of the slab.

During the geometrical optimizations, the upmost three layers and adsorbates were fully relaxed and the bottom layer was fixed. The binding energy ($E_b$) was then obtained by the following equation:

$$E_b = E_{ads/sub} - (E_{sub} + E_{ads}) \tag{4}$$

where the total energy of the adsorbate-substrate system, the clean surface, and the free adsorbate were represented by $E_{ads/sub}$, $E_{sub}$ and $E_{ads}$, respectively.

The reaction free energies were calculated using the computational hydrogen electrode (CHE) model [26]. Each electrochemical reaction step was treated as a simultaneous transfer of the proton-electron pair as a function of the applied potential. The reaction free energies of *steps 1–7* were given by the following equations:

$$\triangle G_{(1)} = G[{*}CO_2] - G[{*}] - G[CO_2] \tag{5}$$

$$\triangle G_{(2)} = G[{*}COOH] - G[{*}CO_2] - G[H^+ + e^-] \tag{6}$$

$$\triangle G_{(3)} = G[{*}CO] + G[H_2O] - G[{*}COOH] - G[H^+ + e^-] \tag{7}$$

$$\triangle G_{(4)} = G[{*}] + G\,[CO] - G[{*}CO] \tag{8}$$

$$\triangle G_{(5)} = G[{*}OCHO] - G[{*}CO_2] - G[H^+ + e^-] \tag{9}$$

$$\triangle G_{(6)} = G[{*}HCOOH] - G[{*}OCHO] - G[H^+ + e^-] \tag{10}$$

$$\triangle G_{(7)} = G[{*}] + G[HCOOH] - G[{*}HCOOH] \tag{11}$$

$$G[H^+ + e^-] = \frac{1}{2}G[H_2] - eU \tag{12}$$

where *U* was the applied overpotential (*vs.* RHE) and e is the elementary charge.

The free energy of different species was calculated according to:

$$G = E_{elec} + E_{ZPE} + \int C_p dT - TS \tag{13}$$

where $E_{elec}$ was the DFT-optimized total energy, $E_{ZPE}$ was the zero-point energy, $C_p$ was the heat capacity and *S* was the entropy. The latter three quantities were calculated from the statistical mechanics within harmonic approximation, taking the vibrational frequencies of adsorbates and molecules as calculated within DFT. We expect the variations in $E_{ZPE}$, $C_p$ and *S* were small compared to the variations in the reaction energies based on $E_{elec}$ alone and assume $E_{ZPE}$, $C_p$ and *S* were constant for all materials considered in this study. We used the values that have been used previously for Cu(211) [27]. The contributions of zero point energy, entropy corrections, and heat capacity to G are summarized in Table S1. The free energy change of the reaction: $CO_2 + H_2 \rightarrow CO + H_2O$ and $CO_2 + H_2 \rightarrow HCOOH$ were fixed at the experimental value of 0.21 eV and 0.45 eV [28], respectively.

## 3. Results and discussion

### 3.1. *Preparation and characterizations of spongeous $Ag_{91}Cu_9$ and coralline $Ag_{65}Cu_{35}$*

Firstly, $Ag_{52}Cu_{39}Sn_9$ alloy foils were obtained by using a single roller melt spinning apparatus, as elucidated in the Method section and Fig. S1. The as-prepared $Ag_{52}Cu_{39}Sn_9$ foils are typically 20–30 μm in thickness, 2–5 mm in width, and several centimeters in length (Fig. S2a). As measured by energy-dispersive X-Ray spectroscopy (EDX) mapping and X-ray photoelectron spectroscopy (XPS) survey (Figs. S2b and c and Fig. S3), the flat surface of the alloy foil is composed of Ag, Cu, and Sn elements. By taking advantage of the ternary metallic components, we then performed an electro-anodizing/dealloying treatment on the $Ag_{52}Cu_{39}Sn_9$ alloy foil to prepare two distinct self-supporting Ag–Cu bimetallic nanostructures with different morphologies and compositions. The anodizing process was employed to selectively etch different metals from the alloy under different potential and electrolyte conditions, as illustrated in Fig. 1a. The atomic ratios of the samples after anodizing were determined by inductively coupled plasma-optical emission spectrometer (ICP-OES) (Table S2). When the $Ag_{52}Cu_{39}Sn_9$ alloy foil was electrochemically etched with an applied potential of 0.3 V (*vs.* saturated calomel electrode, SCE) in 0.5 M aqueous $H_2SO_4$ solution (Figs. S4a and b), Sn atoms and a part of Cu atoms began to dissolve into electrolyte and form structural voids. As more and more sacrificial atoms dispersed into the electrolyte, the inherent stress in the remaining alloy drives the exposed Ag and Cu atoms at the solid/liquid interface segregate into “islands”. After the 3-h anodizing process, the sacrificial elements filling in the interspaces of Ag–Cu islands were completely removed, resulting in the formation of spongeous $Ag_{91}Cu_9$ (Fig. 1b–d). The cross-section scanning electron microscopy (SEM) images of spongeous $Ag_{91}Cu_9$ demonstrate that the $Ag_{52}Cu_{39}Sn_9$ alloy foil was completely etched (Fig. S5). Such a 3D bicontinuous nanostructure was interconnected with numerous nanopores surrounding the Ag–Cu metallic ligaments. Alternatively, $Ag_{52}Cu_{39}Sn_9$ alloy foil was also electrochemically etched in 0.5 M $Na_2SO_4$ aqueous solution (as a neutral dealloying medium) with an applied potential of 0.2 V (*vs.* SCE) for 40 min (Fig. 1a and Figs. S4c and d). After this dealloying process, coralline $Ag_{65}Cu_{35}$ with hierarchical nanodendritic morphology was formed (Fig. 1e–g). In brief, the electrolytes with different pH values were used to obtain distinct Ag–Cu bimetallic nanostructures with different Ag–Cu atomic ratios and morphologies. Most of the Cu atoms in the $Ag_{52}Cu_{39}Sn_9$ alloy foil were electrochemically oxidized to $Cu^{2+}$ ions in acidic environment (0.5 M $H_2SO_4$), while much fewer Cu atoms were etched in neutral medium (0.5 M $Na_2SO_4$). The electrochemical anodizing/etching of Cu could be described via the following reactions (referred in Supporting information):

$$\text{Cathode}: \ 2Cu - 4e^- \xrightarrow{\text{potential}} 2Cu^{2+} \tag{14}$$

$$\text{Anode}: \ 4H^+ + 4e^- \xrightarrow{\text{Potential}} 2H_2\uparrow \tag{15}$$

High-resolution transmission electron microscopy (HRTEM) images of both spongeous $Ag_{91}Cu_9$ (Fig. 1d) and coralline $Ag_{65}Cu_{35}$ (Fig. 1g) exhibit uniform lattice fringes. Selected area electron diffraction (SAED) patterns were taken from broad areas to verify the exposed facets of these samples, respectively, as shown in the insets of Fig. 1d and g. Both SAED patterns exhibit face-centered cubic (FCC) crystal structures similar to metal Ag, since the contents of Ag element predominate in both samples. However, a narrower (111) interplanar spacing of 2.19 Å is observed from coralline $Ag_{65}Cu_{35}$ (Fig. 1g) when compared to that of spongeous $Ag_{91}Cu_9$ (2.36 Å, as presented in Fig. 1d) and metal Ag (2.36 Å). It indicates the increased content of Cu in Ag–Cu alloy leads to a shrinkage of lattice fringe spacing, which is resulted from the rearrangement of Ag and Cu atoms during electrochemical anodizing process.

The crystalline structures and compositions of the samples were characterized (Fig. 2). The X-ray diffraction (XRD) pattern of $Ag_{52}Cu_{39}Sn_9$ alloy foil displays the prominent peaks of metallic Ag (JCPDS card No. 04–0783); meanwhile, meanwhile, the characteristic peaks of Cu (111), Cu (200) and Sn (220) (JCPDS card No. 04–0836 and No. 19–1365) are also detected. After the anodizing processes, the as-prepared spongeous $Ag_{91}Cu_9$ and coralline $Ag_{65}Cu_{35}$ preserve the high crystalline degree and the characteristic peaks of metallic Ag, consistent with the SAED results (the insets of Fig. 1d and g). The crystalline phase of spongeous $Ag_{91}Cu_9$ that contains predominate ratio of Ag atoms is similar to the FCC structure of metallic Ag, since the small amount of Cu atoms might be incorporated into the lattice of Ag; whereas the coralline $Ag_{65}Cu_{35}$ containing higher amount of Cu atoms retains a weak Cu (111) peak. The absence of any diffraction peaks assigned to Cu–Ag alloy phase indicates the phase-segregated nature of the bimetallic samples. Different from the spongeous $Ag_{91}Cu_9$, more slight shifts of XRD peaks can be seen in coralline $Ag_{65}Cu_{35}$ sample, owing to the change of metal compositions. Moreover, the slight shift of the Cu(111) peak position reveals that the Cu and Ag phases together undergone minimal alloying [29]. XPS spectra were further conducted to detect the elemental compositions of spongeous $Ag_{91}Cu_9$ and coralline $Ag_{65}Cu_{35}$, presenting the characteristic peaks of Ag 3d and Cu 2p bands (Fig. 2b and c). As shown in Fig. 2b, the Ag 3d peaks are almost unchanged after the anodizing/etching process, while the Cu 2p peaks of as-etched products shifted to lower energy levels as the content of Ag increases (Fig. 2c). Meanwhile, $Ag_{52}Cu_{39}Sn_9$ exhibits stronger peaks from $Cu^{2+}$ than those of spongeous $Ag_{91}Cu_9$ and coralline $Ag_{65}Cu_{35}$, suggesting $Ag_{52}Cu_{39}Sn_9$ contains more copper oxide on the surface formed during the storage period in ambient atmosphere. The aboved results indicate that the high content of Ag effectively improved the oxidation resistance of remained Cu atoms in the Ag–Cu alloys, therefore much lower signals of surface $Cu^{2+}$ species (with higher binding energy than $Cu^{+}/Cu^{0}$) are observed in the etched products than in the $Ag_{52}Cu_{39}Sn_9$ precursor.

### 3.2. *Electrochemical $CO_2$ reduction performances*

For better comparison, the overall activity of all samples was measured under identical reaction conditions, as detailed in the Methods section. The current density for $CO_2RR$ gradually increases as the applied potential shifts negatively (Fig. 3a). Compared to $Ag_{52}Cu_{39}Sn_9$ alloy foil, the spongeous $Ag_{91}Cu_9$ and coralline $Ag_{65}Cu_{35}$ achieve much higher and steadier current densities at the given potentials ranged from $-0.6$ V to $-1.2$ V (*vs.* reversible hydrogen electrode, RHE), as shown in Figs. S6a–c. To evaluate the influence of competing HER, linear sweep voltammetry (LSV) analysis of the samples was conducted in $CO_2$- and $N_2$-saturated 0.1 M $KHCO_3$ electrolyte, respectively (Fig. S6d). The onset potentials and cathodic currents in $CO_2$-saturated electrolyte are higher than those in $N_2$-saturated electrolyte, suggesting that spongeous $Ag_{91}Cu_9$ and coralline $Ag_{65}Cu_{35}$ prefer to induce $CO_2RR$ rather than HER when the applied potential is more negative than $-0.7$ V (*vs.* RHE).

Since $CO_2RR$ could generate various reduction products, the overall current density should be divided into individual products to get a quantitative assessment of the activity and selectivity. One feasible way is to investigate the respective Faradaic efficiencies of the products, as shown in Fig. 3b–d. By analyzing with gas chromatography (GC) and nuclear magnetic resonance (NMR) techniques (Fig. S7), the products yielded by spongeous $Ag_{91}Cu_9$ and coralline $Ag_{65}Cu_{35}$ are revealed to be mainly composed of HCOOH (in liquid phase), CO and $H_2$ (in gas phase). Over the whole potential range, the trends in Faradaic efficiencies for carbonaceous compounds and for $H_2$ are opposite. Meanwhile, trace

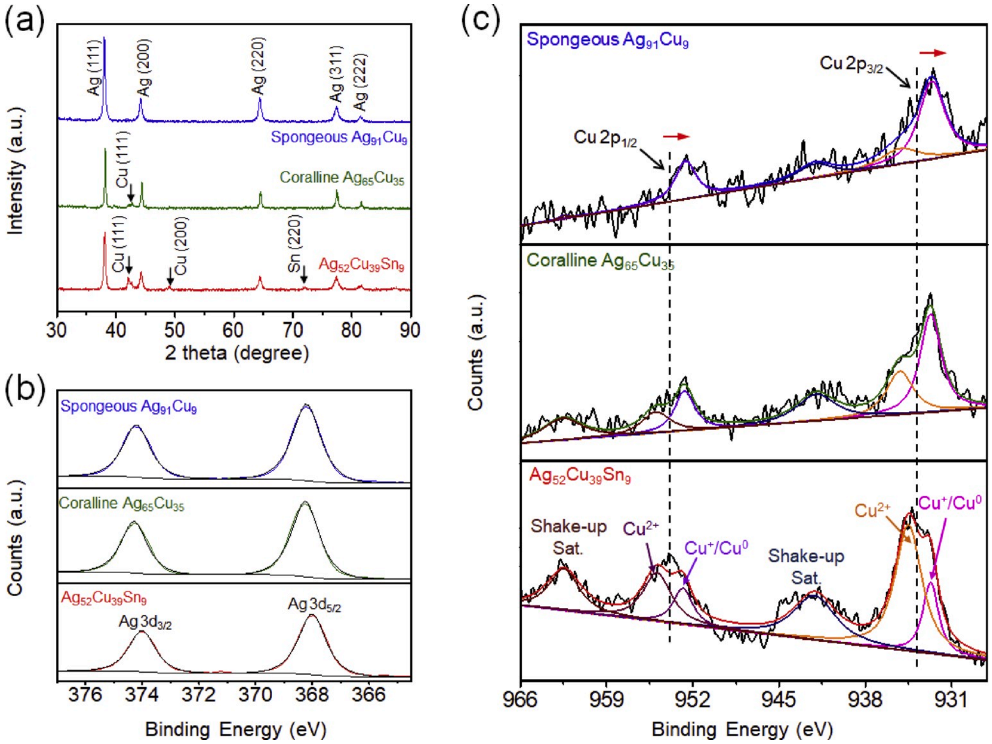

**Fig. 2.** (a) XRD patterns, (b) XPS spectra at Ag 3d region, and (c) XPS spectra at Cu 2p region of spongeous $Ag_{91}Cu_9$, coralline $Ag_{65}Cu_{35}$ and $Ag_{52}Cu_{39}Sn_9$ alloy foil, respectively.

amounts of other hydrocarbon species such as ethanol ($CH_3CH_2OH$), acetone ($CH_3COCH_3$) and acetate ($CH_3COOH$) were also detected (Fig. S8), but the Faradaic efficiencies for these products are less than 1%.

Moreover, as the compositions and geometries of the samples are changed, the product selectivities can be significantly shifted (Fig. 3b–d). As shown in Fig. 3b, with a high atomic ratio of Ag, spongeous $Ag_{91}Cu_9$ achieves an optimal Faradaic efficiency for CO formation ($FE_{CO}$) of 80.6% and delivers a current density of 5.6 mA $cm^{-2}$ at −0.7 V (*vs.* RHE), corresponding to a moderate overpotential of 590 mV (given E°($CO_2$/CO) = −0.11 V *vs.* RHE) [30]. While at −0.6 V (*vs.* RHE), spongeous $Ag_{91}Cu_9$ shows a $FE_{CO}$ of 54.4% with HER acting as an obvious side reaction, which indicates that the overpotential is relatively low to drive $CO_2RR$ energetically enough to compete with HER. As the potential changes from −0.8 V to −1.1 V (*vs.* RHE), the $FE_{CO}$ of spongeous $Ag_{91}Cu_9$ gradually decreases and considerable amounts of $H_2$ and formate are detected. With the further increase of overpotential, the $FE_{CO}$ of spongeous $Ag_{91}Cu_9$ drops to below 50% at −1.2 V (*vs.* RHE), which is most probably due to the mass transport limitation of $CO_2$ molecules at relatively high current densities, rather than the intrinsic activity limitation of electrocatalyst.

By tuning the atomic compositions and geometries of samples, the Faradaic efficiencies of different electro-reduction products were changed. As shown in Fig. 3c, coralline $Ag_{65}Cu_{35}$ with a higher content of Cu atoms exhibits high selectivity towards formate production, which is one of the main liquid-phase products of Cu-based electrocatalysts [31]. The product selectivity of coralline $Ag_{65}Cu_{35}$ towards formate and $H_2$ is dependent on the applied potential, while the $FE_{CO}$ is relatively low and has only little change varied with the potential. At −0.6 V (*vs.* RHE), coralline $Ag_{65}Cu_{35}$ shows a Faradaic efficiency for formate formation ($FE_{formate}$) of only 26.6%, owing to the completion of HER under a small applied potential. When the potential reaches −0.8 V (*vs.* RHE), the $FE_{formate}$ of coralline $Ag_{65}Cu_{35}$ quickly rises to 68.0% and the $H_2$ production rate drops sharply. When the potential is set in the range from −0.9 to −1.2 V (*vs.* RHE), the $FE_{formate}$ of coralline $Ag_{65}Cu_{35}$ further increases to higher levels. At −1.0 V (*vs.* RHE), the $FE_{formate}$ of coralline $Ag_{65}Cu_{35}$ reaches a peak value of 91.8%, and the selectivity of formate is up to 86.0% with a high current density of 18.3 mA $cm^{-2}$; meanwhile, the Faradaic efficiency for $H_2$ by-product ($FE_{H2}$) is effectively suppressed to a minimal value (~2.9%). At the potentials of −1.1 and −1.2 V (*vs.* RHE), the $FE_{formate}$ of coralline $Ag_{65}Cu_{35}$ declines slightly and the $FE_{H2}$ is kept at around 8%.

In contrast, as a control sample, $Ag_{52}Cu_{39}Sn_9$ alloy foil exhibits poor product selectivities for carbonaceous compounds (Fig. 3d), much inferior to those of spongeous $Ag_{91}Cu_9$ or coralline $Ag_{65}Cu_{35}$ at the same potentials, because the HER acts as a conspicuous competing reaction on the surface of $Ag_{52}Cu_{39}Sn_9$.

The $FE_{CO}$, $FE_{formate}$, $FE_{H2}$, partial current density for CO production ($J_{CO}$) and partial current density for formate production ($J_{formate}$) of these three samples at −0.7 V and −1.0 V (*vs.* RHE) are summarized in Fig. S9, respectively. Observed from Fig. S9a, spongeous $Ag_{91}Cu_9$ achieves the highest $FE_{CO}$ (80.6%) at −0.7 V (*vs.* RHE), which is far beyond coralline $Ag_{65}Cu_{35}$ (10.6%) and $Ag_{52}Cu_{39}Sn_9$ (5.4%). Moreover, spongeous $Ag_{91}Cu_9$ also reaches the highest $J_{CO}$ (4.52 mA $cm^{-2}$) at −0.7 V (*vs.* RHE), much higher than the values of coralline $Ag_{65}Cu_{35}$ (0.32 mA $cm^{-2}$) and $Ag_{52}Cu_{39}Sn_9$ (0.02 mA $cm^{-2}$), as shown in Fig. S9C. When the potential shifts to −1.0 V (*vs.* RHE), the $FE_{formate}$ of these samples are all increased (Fig. S9b). Among them, coralline $Ag_{65}Cu_{35}$ exhibits the best selectivity for formate production and achieves the highest $FE_{formate}$ of 91.8%, while the other two samples show relatively low values. Meanwhile, coralline $Ag_{65}Cu_{35}$ exhibits the largest $J_{formate}$ (16.79 mA $cm^{-2}$) at −1.0 V (*vs.* RHE), which is 4.5 and 10.8 times higher than those of spongeous $Ag_{91}Cu_9$ (3.67 mA $cm^{-2}$) and $Ag_{52}Cu_{39}Sn_9$ (1.55 mA $cm^{-2}$), respectively (Fig. S9d). The improved $CO_2RR$ activity and tunable selectivity of spongeous $Ag_{91}Cu_9$ and coralline $Ag_{65}Cu_{35}$ mainly result from the modulating of compositions and electron structures, which effectively lower the energy barrier for $CO_2$ activation and tune the binding strength of reaction intermediates. Table S3 summarized the performances of other typical metal-based electrocatalysts in the literature [31–37] for the comparison with spongeous $Ag_{91}Cu_9$ and coralline

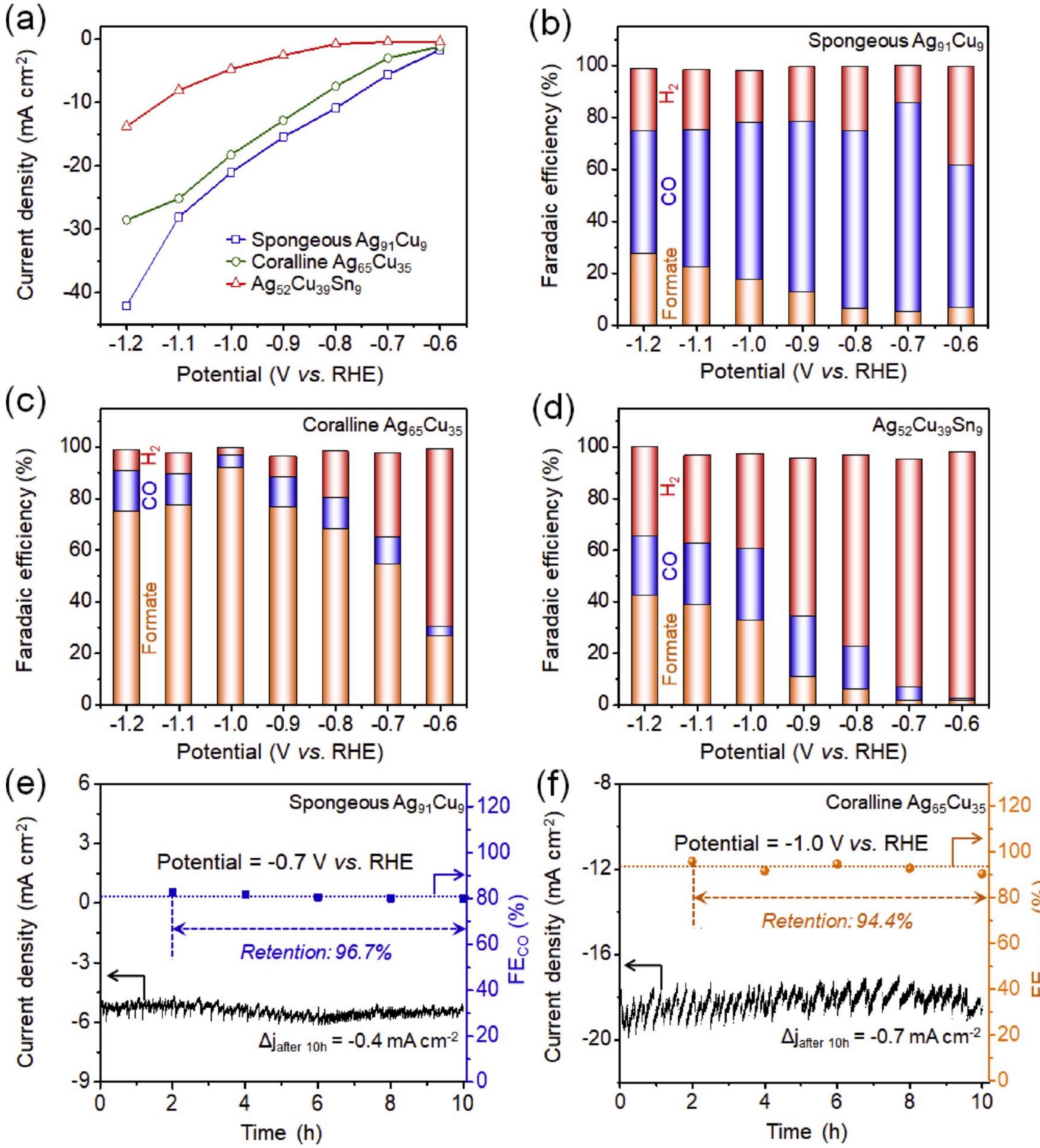

**Fig. 3.** (a) Comparison of geometric current densities of the samples as a function of applied potential. (b–d) Faradaic efficiencies of the reduction products generated by (b) spongeous $Ag_{91}Cu_9$, (c) coralline $Ag_{65}Cu_{35}$ and (d) $Ag_{52}Cu_{39}Sn_9$ alloy foil in $CO_2$-saturated 0.1 M $KHCO_3$ aqueous solution at different potentials for 4 h. (e, f) Long-term chronopotentiometric $CO_2RR$ tests of (e) spongeous $Ag_{91}Cu_9$ at −0.7 V (*vs.* RHE) and (f) coralline $Ag_{65}Cu_{35}$ at −1.0 V (*vs.* RHE), respectively.

$Ag_{65}Cu_{35}$, showing that the bicontinuous porous Ag–Cu nanoarchitectures possess good catalytic activity and selectivity towards $CO_2$-to-CO/formate conversion.

To further investigate the operation stability of bicontinuous porous Ag–Cu electrocatalysts, long-term $CO_2RR$ tests were performed, as shown in Fig. 3e and f. During the entire working process for 10 h at −0.7 V (vs. RHE), the $FE_{CO}$ of spongeous $Ag_{91}Cu_9$ shows a high retention of 96.7% (Fig. 3e). The current density shows some fluctuations over time, owing to the generation, accumulation and desorption of gas bubbles on the electrode surface. After long-term electrocatalysis test, the structural and surface composition variations of spongeous $Ag_{91}Cu_9$ were measured by SEM, XRD and XPS characterizations (Fig. S10). No obvious structure collapse or ingredient changes are observed, revealing that the structural stability of spongeous $Ag_{91}Cu_9$ are well maintained during the test. Similarly, coralline $Ag_{65}Cu_{35}$ also shows good long-term stability for $CO_2RR$ at an applied potential of −1.0 V (vs. RHE) (Fig. 3f). The $FE_{formate}$ of coralline $Ag_{65}Cu_{35}$ keeps at above 90% and the current density presents very small decrease during the 10-h test. The SEM, XRD and XPS analyses after long-term $CO_2RR$ test confirm that coralline $Ag_{65}Cu_{35}$ has no appreciable structural change (Fig. S11). These results reveal that the spongeous $Ag_{91}Cu_9$ and coralline $Ag_{65}Cu_{35}$ electrocatalysts exhibit high operation stability for $CO_2RR$.

### 3.3. *In-situ Raman spectroscopic analysis*

To evaluate the electrochemical kinetics performances of spongeous $Ag_{91}Cu_9$ and coralline $Ag_{65}Cu_{35}$ for the electroreduction of $CO_2$ into carbonaceous products, ECSA measurements and Tafel analysis were conducted. As shown in Fig. S12, the corresponding ECSA of these three samples show significant differences. The ECSA values of spongeous $Ag_{91}Cu_9$ and coralline $Ag_{65}Cu_{35}$ are ~71.3 times and ~57.3 times higher than that of $Ag_{52}Cu_{39}Sn_9$ alloy foil, respectively, which is attributed to the much larger amounts of active sites exposed on the highly-curved surfaces of spongeous $Ag_{91}Cu_9$ and coralline $Ag_{65}Cu_{35}$ after anodizing treatment. The enlarged ECSA enables rapid electron transfer for accelerating the formation of reaction intermediates towards CO/formate production. Therefore, compared to the flat $Ag_{52}Cu_{39}Sn_9$ alloy foil, spongeous $Ag_{91}Cu_9$ and coralline $Ag_{65}Cu_{35}$ could realize much faster reaction kinetics for $CO_2$RR. However, the distinct product selectivity of spongeous $Ag_{91}Cu_9$ and coralline $Ag_{65}Cu_{35}$ does not come from the different ECSA values, but from the variation of surface atomic and electronic structures. The intrinsic electrodynamics of two-electron $CO_2$ reduction on these electrocatalysts were further analyzed by the Tafel slops (Fig. 4a and b), and the calculated $J_{CO}$ and $J_{formate}$ are also presented in Table S4 and Table S5, respectively. As shown in Fig. 4a, the Tafel slopes for CO formation on spongeous $Ag_{91}Cu_9$ and coralline $Ag_{65}Cu_{35}$ are 73.3 mV $dec^{-1}$ and 119.4 mV $dec^{-1}$, respectively. By comparison, the lower Tafel slope of spongeous $Ag_{91}Cu_9$ suggests that it facilitates the conversion of $CO_2$ into CO more effectively than coralline $Ag_{65}Cu_{35}$. Meanwhile, the largest Tafel slope of 124.6 mV $dec^{-1}$ for $Ag_{52}Cu_{39}Sn_9$ suggests the $CO_2$ activation on the flat surface is quite inferior [37]. When it refers the Tafel analysis for formate production (Fig. 4b), coralline $Ag_{65}Cu_{35}$ exhibits the lowest Tafel slope (117.1 mV $dec^{-1}$) among these samples. In comparison, spongeous $Ag_{91}Cu_9$ and $Ag_{52}Cu_{39}Sn_9$ show much higher Tafel slopes for formate production (254.0 and 155.8 mV $dec^{-1}$, respectively), indicates their inferior reaction kinetics towards $CO_2$-to-formate conversion.

To understand the origins of catalytic activity for $CO_2$RR, it is necessary to gain a fundamental insight into the real-time interfacial processes and the formed reaction intermediates on the surface of electrocatalyst by *in-situ* spectroscopic measurements. Fig. 4c and d shows the *in-situ* Raman spectra collected on spongeous $Ag_{91}Cu_9$ in a spectroelectrochemical cell (Fig. S13). The black curves were measured in the $CO_2$-saturated 0.1 M $KHCO_3$ solution before electrolysis (without applied potential). The Raman peak at 588 $cm^{-1}$ is assigned to the $Cu_2O$ on the surface of spongeous $Ag_{91}Cu_9$ formed by exposed to air. After the

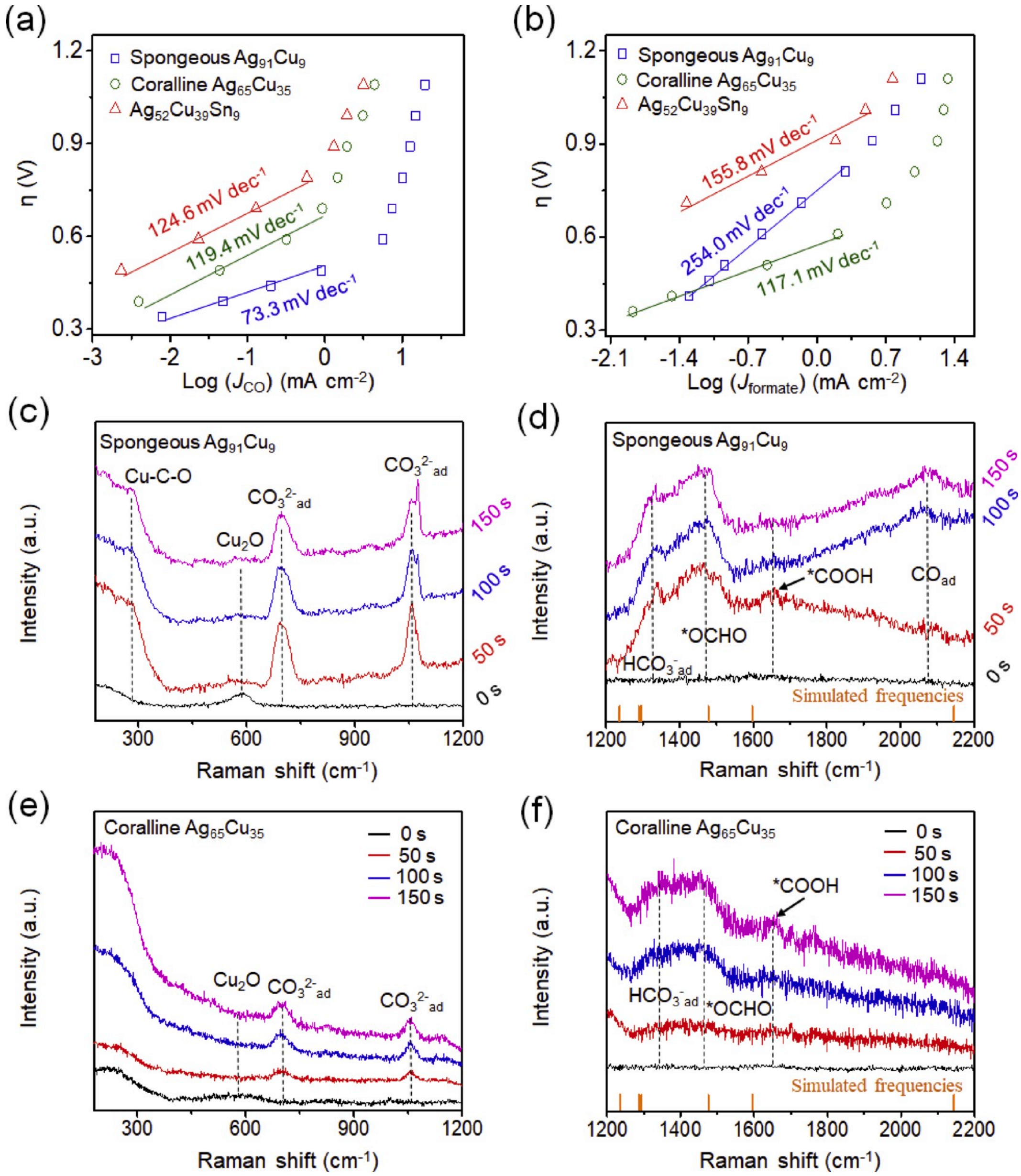

**Fig. 4.** (a, b) Tafel slopes of the samples for (a) CO production and (b) formate production. (c–f) Time-dependent *in-situ* Raman spectra recorded from the surface of (c, d) spongeous $Ag_{91}Cu_9$ and (e, f) coralline $Ag_{65}Cu_{35}$. The orange-color sticks in (d) and (f) represent the DFT-calculated vibrational frequencies (in $cm^{-1}$) of different vibration models for *COOH, *OCHO and CO species.

potential of −0.7 V (*vs.* RHE) has been applied for 50 s, the characteristic peak originated from $Cu_2O$ show a significant intensity decrease, which is owing to the electroreduction of $Cu_2O$ surface layer. Meanwhile, some other Raman peaks are emerged and exhibit strong peak intensities, owing to the surface-enhanced Raman scattering (SERS) or inelastic light scattering by electron-hole plasma in the alloy [38]. The peaks at 697 $cm^{-1}$ and 1058 $cm^{-1}$ correspond to the vibrational modes of $CO_3^{2-}$ in aqueous solution [39,40] and the peak at 1340 $cm^{-1}$ is attributed to the $HCO_3^-$ in the electrolyte. Nevertheless, the $CO_3^{2-}$ and $HCO_3^-$ don't act as active species in the $CO_2RR$ since there is no carbonaceous products could be generated in $N_2$-saturated 0.1 M $KHCO_3$ solution. Moreover, the *in-situ* Raman spectra also provide valuable information of the reaction intermediates formed during the $CO_2RR$. The peak emerged at 267 $cm^{-1}$ is assigned to Cu–C–O bending and represents the surface-bound CO intermediates on the Cu [20]. In spongeous $Ag_{91}Cu_9$, the higher proportion of Ag acts as an energetical promoter that generates a higher flux of CO, and thus, adjacent Cu atoms could have more opportunity to adsorb *CO intermediates. However, gaseous CO could be hardly generated on Cu sites since the binding energy of *CO on Cu atoms is relatively high. The broad peak at 1469 $cm^{-1}$ is assigned to the symmetric stretching vibration of the carboxylate group (namely, υ-O-(CH)-O), corresponding to the surface-adsorbed *OCHO intermediates [40]. The weak peak at 1650 $cm^{-1}$ belongs to the *COOH intermediates [41], and the peak at 2076 $cm^{-1}$ is attributed to the molecular CO bound on the catalyst surface [42], which indicates the relationship between *COOH intermediates and CO product. The theoretical vibrational frequencies of *COOH, *OCHO and CO species are also calculated by DFT simulation (Table S6). The shift of Raman peak

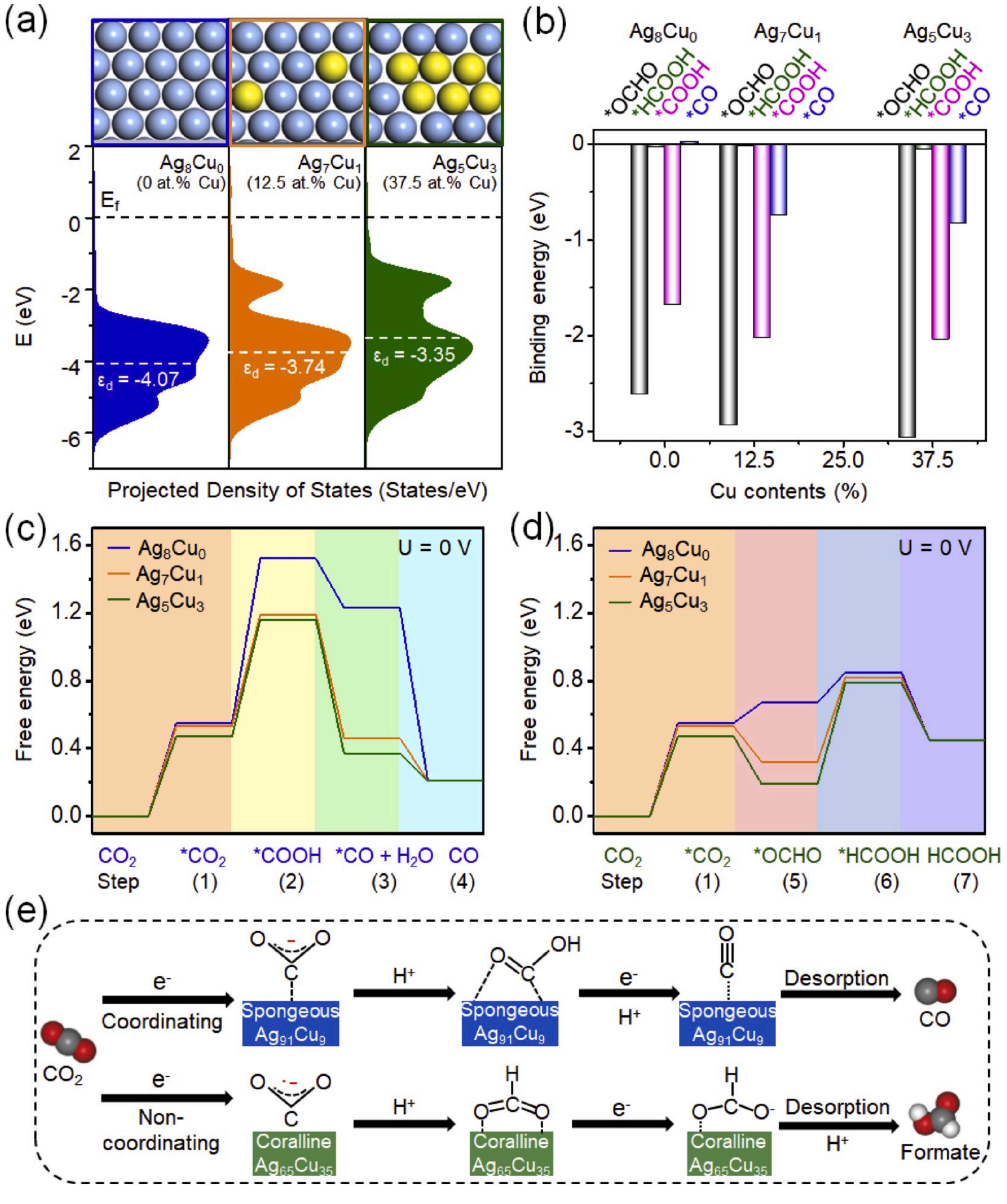

**Fig. 5.** (a) Calculated d-band electronic states of surface atoms on $Ag_8Cu_0(111)$, $Ag_7Cu_1(111)$ and $Ag_5Cu_3(111)$ with varying extents of Cu enrichments. The black dashed line represents the Fermi level ($E_f$) and the white dashed lines indicate the d-band centers ($\varepsilon_d$). (b) The calculated binding energies of *OCHO, *HCOOH, *COOH and *CO species adsorbed on Ag–Cu surfaces with different Cu contents. Reaction free energetics of the (c) $CO_2$-to-CO and (d) $CO_2$-to-formate pathways for $CO_2RR$ on $Ag_8Cu_0(111)$, $Ag_7Cu_1(111)$ and $Ag_5Cu_3(111)$ interfaces. (e) Proposed dominating reaction pathways on spongeous $Ag_{91}Cu_9$ and coralline $Ag_{65}Cu_{35}$, respectively.

positions is rationalized by the chemisorption of different intermediates/molecules on metal/alloy surface. For example, when a CO molecule is bound on a metal surface, it is expected that the electron is donated from the CO 5$\sigma$ molecular orbital to the metal surface, and also from the metal surface back to the CO 2$\pi$* antibonding orbital, which decreases the strength of the C–O bond [39]. As a result, the observed frequencies of adsorbed CO are lower than that of gaseous CO. As the operation time goes up to 100 and 150 s, the *COOH band gradually disappears, while the peak intensity of molecular CO greatly enhances, suggesting that the *COOH intermediates play a key role for the $CO_2$-to-CO conversion. The $CO_2$ molecules adsorb on spongeous $Ag_{91}Cu_9$ electrode are reduced to *COOH species at first, and then the *COOH species are further reduced to *CO intermediates. These results verify that the spongeous $Ag_{91}Cu_9$ electrode preferentially generates CO as the main product through the reaction pathway of $CO_2$ → *COOH → *CO → CO. As a comparison, the *in-situ* Raman spectra measured on coralline $Ag_{65}Cu_{35}$ at −1.0 V (*vs.* RHE) are shown in Fig. 4e and f. The peak observed at 1469 $cm^{-1}$ is assigned to the O-(CH)-O bending of *OCHO intermediates (Fig. 4f), which could be further reduced to *HCOOH species, and then results in the production of formate. Meanwhile, the *COOH signal at 1650 $cm^{-1}$ is very weak until reacted for 150 s, and the peaks belonging to Cu–C–O and molecular CO are scarcely observed, indicating that the amount of CO produced on coralline $Ag_{65}Cu_{35}$ is very low.

### 3.4. Mechanism analysis of electronic structure modulation by varying the Ag–Cu ratios

To understand the synergistic influence of electronic and geometric effects on the product selectivity when the surface compositions of Ag–Cu nanoarchitectures shift, the possible reaction pathways were analyzed by DFT calculations. A series of optimized Ag–Cu alloy configurations with varying Cu contents (Fig. 5a), i.e. $Ag_8Cu_0$, $Ag_7Cu_1$, and $Ag_5Cu_3$ were adopted to explore the reaction trends towards CO/formate production. The simulation of $CO_2RR$ pathways were performed on the (111) surfaces since they are the predominantly exposed and stable crystal planes, as evidenced by both SAED patterns (the insets in Fig. 1d and g) and DFT calculations (Table S7 and Fig. S14). As shown in Fig. 5a, the calculated projected density of states (PDOS), which describes the electronic states at the metal surfaces, demonstrates that the Ag–Cu alloying could lead to distinct electronic properties form pure Ag. Once the electronic density of the metal center in alloy changes to an appropriate value to match the energy level of reactant species, electrons will be easily transferred to activate $CO_2$ molecules and initiate the catalytic reaction. More importantly, the changes in d-band structure brings about the electronic effects on the binding strength of intermediates. This allows the Ag–Cu alloys with different compositions to exhibit distinct catalytic activities. Fig. 5a reveals that the d-band center ($\varepsilon_d$) gradually shift upwards as the Ag content decreases. From the view of the electronic effect, when the degree of alloying increases, the $\varepsilon_d$ tends to up-shift closer to the Fermi level and results in stronger adsorbates-metal interaction [43]. According to this trend, the binding strengths for *COOH and *CO are supposed to increase as the Ag content decreases, which suggests that the desorption of CO becomes more difficult as more Cu atoms are introduced into Ag–Cu alloys. Moreover, the binding energies ($E_b$) of reaction intermediates and the Gibbs free energy changes ($\Delta G$) of elementary steps in $CO_2RR$ at a potential ($U = 0$ V) were calculated. Fig. 5b and Table S8 show the calculated $E_b$ of *OCHO, *HCOOH, *COOH, and *CO reaction intermediates involved in $CO_2RR$ on $Ag_8Cu_0$(111), $Ag_7Cu_1$(111) and $Ag_5Cu_3$(111) surfaces. The *CO intermediates bind more strongly on $Ag_7Cu_1$(111) and $Ag_5Cu_3$(111) surfaces than on pure $Ag_8Cu_0$(111) surface, which makes the desorption more difficult at the "mixed" sites, and thus suppresses the CO production when the Cu content increases to a high level. Combined with the geometric effect, as the alloy compositions shift, the atomic rearrangement of reaction sites will also change, which could influence the formation free-energies and the adsorption capacities of reaction intermediates (Fig. S15 and Fig. 5c and d). The Ag atoms on $Ag_8Cu_0$(111) and $Ag_7Cu_1$(111) act as the main active sites, while the Cu and Ag atoms on $Ag_5Cu_3$(111) surface work cooperatively to bind the reaction intermediates (Fig. S15). For $CO_2$-to-CO conversion, the *CO intermediates binds weakly on $Ag_8Cu_0$(111) surface, which makes the CO desorption downhill in energy by 1.02 eV ($\Delta G$(CO) - $\Delta G$(*CO)) (Fig. 5c), contributing to a highly exothermic and spontaneous step. In contrast, the formation of *OCHO on $Ag_8Cu_0$(111) is considered as a difficult step and is uphill in $\Delta G$ by 0.12 eV ($\Delta G$(*OCHO) - $\Delta G$(*$CO_2$)), as shown in Fig. 5d. These results coincide with the experimental observations of metallic Ag as a favorable choice for CO production [35]. Accordingly, when Ag dominates in Ag–Cu bimetallic catalyst, the main product of $CO_2RR$ will be CO. In contrast, the formation of *OCHO on $Ag_7Cu_1$(111) and $Ag_5Cu_3$(111) is a spontaneous and exothermic process. Through the consecutive proton/electron transfer, $Ag_5Cu_3$(111) maintains the lowest reaction free energetics for the $CO_2$-to-formate pathway, indicates that the energetic catalytic activities for formate production are primarily attributable to the increased abundance of Ag–Cu (111) facets. This demonstrates that the introduction of Cu atoms can enhance the catalytic activity and tune the product selectivity of Ag–Cu alloy to generate formate, which are in good agreement with the experimental results.

According to the above analysis, the proposed dominating pathways via different reaction intermediates on spongeous $Ag_{91}Cu_9$ and coralline $Ag_{65}Cu_{35}$ are illustrated in Fig. 5e, respectively. In detail, the elementary steps are listed below:

$$* + CO_2\ (g) \rightarrow *CO_2\ (ads.) \qquad \text{(Step 1)}$$

$$*CO_2\ (ads.) + H^+ + e^- \rightarrow *COOH\ (ads.) \qquad \text{(Step 2)}$$

$$*COOH\ (ads.) + H^+ + e^- \rightarrow *CO\ (ads.) + H_2O\ (l) \qquad \text{(Step 3)}$$

$$*CO\ (ads.) \rightarrow * + CO\ (g) \qquad \text{(Step 4)}$$

$$*CO_2\ (ads.) + H^+ + e^- \rightarrow *OCHO\ (ads.) \qquad \text{(Step 5)}$$

$$*OCHO\ (ads.) + H^+ + e^- \rightarrow *HCOOH\ (ads.) \qquad \text{(Step 6)}$$

$$*HCOOH\ (ads.) \rightarrow * + HCOOH\ (l) \qquad \text{(Step 7)}$$

where '*' represents the surface adsorption site on electrode. For spongeous $Ag_{91}Cu_9$, the adsorbed $CO_2$ molecule is initially absorbed on the surface and the activated to *$CO_2$ intermediates. Coupled with a simultaneous proton/electron transfer, the *COOH intermediates are formed and bound on the catalyst surface (Step 2). Through the second proton/electron transfer, the generated *CO species easily desorbs from the electrode, promoting the release of gaseous CO as the dominant product (Step 3 and 4). Moreover, because the Ag content in spongeous $Ag_{91}Cu_9$ is high, the inherent stress could drive Ag atoms to segregate into islands, and thus the main product of $CO_2RR$ will be CO since Ag acts as the active promoter for *CO intermediate desorption. Differently, on the surface of coralline $Ag_{65}Cu_{35}$, the main product of formate would be generated through the energetically favorable formation of *OCHO adsorbates (Step 5) and the subsequent desorption of *HCOOH intermediates (Step 6 and 7).

Notably, trace amounts of other hydrocarbon species such as $CH_3CH_2OH$, $CH_3COCH_3$ and $CH_3COOH$ were detected during the $CO_2RR$, and the yields of multi-carbon ($C_2$ and $C_3$) products generated by coralline $Ag_{65}Cu_{35}$ are slightly higher than those of spongeous $Ag_{91}Cu_9$ (Fig. S8), which could be attributed to the enhanced CO adsorption on coralline $Ag_{65}Cu_{35}$ (Table S8). However, the selectivity towards $C_2$–$C_3$ products on coralline $Ag_{65}Cu_{35}$ is still very low, owing to its relatively low surface coverage ratio of Cu atoms compared to pristine Cu metal that hiders the subsequent CO–CO dimerization and its predominately exposed Ag–Cu (111) facets, as evidenced by the XRD pattern (Fig. 2a). It has been reported that Cu (111) facets are conducive to the selective production of $C_1$ chemicals whereas Cu (100) facets favor $C_2$ products, since CO–CO dimerization prefers to proceed on Cu

(100) in both kinetics and thermodynamics when compared to Cu (111) [44]. Meanwhile, Cu (110) and (220) facets also favor the formation of $C_2$ products as compared to Cu (100) and (111) surfaces, due to the higher *CO binding energies and the lower CO–CO coupling barriers [45]. Following this line of thought, we suggest that the yield of $C_2$ products can be increased by taking advantage of high-index facets or atomic steps located on Cu (111) basal planes. To prove it, nanoporous Cu was prepared as a control sample for the $CO_2RR$ by electrochemical dealloying/etching of commercial $Cu_{60}Zn_{40}$ alloy foil, as presented in the Method section and Figs. S16–20. The SEM images of nanoporous Cu clearly display its high porosity (Fig. S18), and the complete removal of Zn is confirmed by EDX, XRD and XPS characterizations (Fig. S19). Besides Cu (111) facets, the characteristic peaks of Cu (200) and Cu (220) are also detected in nanoporous Cu, as confirmed by XRD (Fig. S19b). The $CO_2RR$ products of nanoporous Cu at different potentials is summarized in Fig. S20b. $H_2$, formate and CO account for a high proportion of the reaction products generated by nanoporous Cu, and the formation of different hydrocarbon products via multi-electron reduction processes are also detected, including methane ($CH_4$), ethylene ($C_2H_4$) and $CH_3CH_2OH$, further verifying that the geometric and electronic structures of electrocatalyst can greatly influence its catalytic activity and selectivity.

## 4. Conclusions

In summary, we have developed an efficient electrochemical anodizing/etching approach to prepare self-supporting Ag–Cu alloy nanostructures for electrochemical $CO_2RR$. The bicontinuous and hierarchical porous morphology of spongeous $Ag_{91}Cu_9$ and coralline $Ag_{65}Cu_{35}$ catalysts could expose abundant active sites to promote $CO_2$ adsorption and electron transfer capability. The surface compositions and atomic arrangement of bimetallic catalysts synergistically determine the reaction pathway and main products, realizing highly activity and tunable selectivity. Analyzed by *in-situ* Raman measurements and theoretical calculations, the variations in the electronic structure and surface atoms of the catalyst can modulate the formation free-energies and binding strength of different reaction intermediates, and thus, different product selectivities are realized. We believe this work could provide a promising route for the rational design of nanostructural electrocatalysts that can be produced by electrochemical dealloying methods with improved activity, selectivity and durability towards $CO_2$ reduction and re-utilization.

## Declaration of competing interest

The authors declare that they have no known competing financial interests or personal relationships that could have appeared to influence the work reported in this paper.

## Acknowledgements

This work was supported by National Key R&D Program of China (2017YFA0208200, 2016YFB0700600), Projects of NSFC (21872069, 51761135104, 21573108), Natural Science Foundation of Jiangsu Province (BK20180008), High-Level Innovative and Entrepreneurial Program of Jiangsu Province, and the Fundamental Research Funds for the Central Universities of China (0205-14380188).

## Appendix A. Supplementary data

Supplementary data to this article can be found online at https://doi.org/10.1016/j.nanoen.2020.104796.

## References

[1] P.M. Cox, R.A. Betts, C.D. Jones, S.A. Spall, I.J. Totteredell, Nature 408 (2000) 184–187.
[2] S. Solomon, G.K. Plattner, R. Knutti, P. Friedlingstein, Geophys. Proc. Natl. Acad. Sci. 106 (2009) 1704–1709.
[3] M.I. Hoffert, K. Caldeira, G. Benford, D.R. Criswell, C. Green, H. Herzog, A.K. Jain, H.S. Kheshigi, K.S. Lackner, J.S. Lewis, H.D. Lightfoot, W. Manheimer, J. C. Mankins, M.E. Mauel, L.J. Perkins, M.E. Schlesinger, T. Volk, T.M. Wigley, Science 298 (2002) 981–987.
[4] J. Khan, M.H. Arsalan, Renew. Sust. Energ. Rew. Electrochem. 55 (2016) 414–425.
[5] J. Yang, B. Chen, Appl. Energy 177 (2016) 239–246.
[6] J.Y. Kim, T.A. Johnson, J.E. Miller, E.B. Stechel, C.T. Maravelias, Energy Environ. Sci. 5 (2012) 8417–8429.
[7] B. Zaidman, H. Wiener, Y. Sasson, Int. J. Hydrogen Energy 11 (1986) 341–347.
[8] X.W. Yu, P.G. Pickup, J. Power Sources 182 (2008) 124–132.
[9] F. Jiao, J.J. Li, X.L. Pan, J.P. Xiao, H.B. Li, H. Ma, M.M. Wei, Y. Pan, Z.Y. Zhou, M. R. Li, S. Miao, J. Li, Y.F. Zhu, D. Xiao, T. He, J.H. Yang, F. Qi, Q. Fu, X.H. Bao, Science 351 (2016) 1065–1068.
[10] H.T. Luk, C. Mondelli, D.C. Ferré, J.A. Stewart, J. Pérez-Ramírez, Chem. Soc. Rev. 46 (2017) 1358–1426.
[11] W. Knorr, Geophys. Res. Lett. 36 (2009) L21710.
[12] H.R.M. Jhong, S.C. Ma, P.J. Kenis, Curr. Opin. Chem. Eng. 2 (2013) 191–199.
[13] W.J. Zhang, Y. Hu, L.B. Ma, G.Y. Zhu, Y.R. Wang, X.L. Xue, R.P. Chen, S.Y. Yang, Z. Jin, Adv. Sci. 5 (2017) 1700275.
[14] J. Greeley, T.F. Jaramillo, J. Bonde, I. Chorkendorff, J.K. Nørskov, Nat. Mater. 5 (2006) 909–913.
[15] H.A. Hansen, J.B. Varley, A.A. Peterson, J.K. Nørskov, J. Phys. Chem. Lett. 4 (2013) 388–392.
[16] A.A. Peterson, J.K. Nørskov, J. Phys. Chem. Lett. 3 (2012) 251–258.
[17] C.J. Lei, Y. Wang, Y. Hou, P. Liu, J. Yang, T. Zhao, X.D. Zhuang, M.W. Chen, L. C. Lei, C. Yuan, M. Qiu, X.L. Feng, Energy Environ. Sci. 12 (2019) 149–156.
[18] H.K. Lim, H.Y. Shin, W.A. Goddard, Y.J. Hwang, B.K. Min, H.J. Kim, J. Am. Chem. Soc. 136 (2014) 11355–11361.
[19] J.F. He, K.E. Dettelbach, A.X. Huang, C.P. Berlinguette, Angew. Chem. Int. Ed. 129 (2017) 16806–16809.
[20] T.T.H. Hoang, S. Verma, S.C. Ma, T.T. Fister, J. Timoshenko, A.I. Frenkel, P.J. A. Kenis, A.A. Gewirth, J. Am. Chem. Soc. 140 (2018) 5791–5797.
[21] H.S. Hou, M.J. Jing, Y.C. Yang, Y. Zhang, Y.R. Zhu, W.X. Song, X.M. Yang, X.B. Ji, J. Mater. Chem. A 3 (2015) 2971–2977.
[22] S. Liu, J.K. Feng, X.F. Bian, J. Liu, H. Xu, Energy Environ. Sci. 9 (2016) 1229–1236.
[23] L.Y. Liang, Y. Xu, C.L. Wang, L.Y. Wen, Y.G. Fang, Y. Mi, M. Zhou, H.P. Zhao, Y. Lei, Energy Environ. Sci. 8 (2015) 2954–2962.
[24] J.H. Koh, D.H. Won, T. Eom, N.K. Kim, W.D. Jung, H.J. Kim, Y.J. Hwang, B.K. Min, ACS Catal. 7 (2017) 5071–5077.
[25] T. Fujita, P.F. Guan, K. Mckenna, X.Y. Lang, A. Hirata, L. Zhang, T. Tokunaga, S. Arai, Y. Yamamoto, N. Tanaka, Y. Ishikawa, N. Asao, Y. Yamamoto, J. Erlebacher, M.W. Chen, Nat. Mater. 11 (2012) 775–780.
[26] J.K. Nørskov, J. Rossmeisl, A. Logadottir, L. Lindqvist, J. Phys. Chem. B 108 (2004) 17886–17892.
[27] A.A. Peterson, F. Abild-Pedersen, F. Studt, J. Rossmeisl, J.K. Nørskov, Energy Environ. Sci. 3 (2010) 1311–1315.
[28] J.A. Dean, Lange's Handbook of Chemistry, McGraw-Hill, Inc. Press, New York; London, 1999.
[29] E.L. Clark, C. Hahn, T.F. Jaramillo, A.T. Bell, J. Am. Chem. Soc. 139 (2017) 15848–15857.
[30] J.Q. Xu, X.D. Li, W. Liu, Y.F. Sun, Z.Y. Ju, T. Yao, C.M. Wang, H.X. Ju, J.F. Zhu, S. Q. Wei, Y. Xie, Angew. Chem. Int. Ed. 56 (2017) 9121–9125.
[31] J. Chung, D.H. Won, J. Koh, E. Kim, S.I. Woo, Phys. Chem. Chem. Phys. 18 (2016) 6252–6258.
[32] D. Kim, J. Resasco, Y. Yu, A.M. Asiri, P.D. Yang, Nat. Commun. 5 (2014) 1–8.
[33] S. Rasul, D.H. Anjum, A. Jedidi, Y. Minenkov, L. Cavallo, K. Takanabe, Angew. Chem. Int. Ed. 54 (2015) 2146–2150.
[34] S. Sarfraz, A.T. Garcia-Esparza, A. Jedidi, L. Cavallo, K. Takanabe, ACS Catal. 6 (2016) 2842–2851.
[35] Q. Lu, J. Rosen, Z. Yang, G.S. Hutchings, Y.C. Kimmel, J.G. Chen, F. Jiao, Nat. Commun. 5 (2014) 3242.
[36] R. Kortlever, I. Peters, S. Koper, M.T.M. Koper, ACS Catal. 5 (2015) 3916–3923.
[37] F.W. Li, M.Q. Xue, J.Z. Li, X.L. Ma, L. Chen, X.J. Zhang, D.R. Macfarlane, J. Zhang, Angew. Chem. Int. Ed. 129 (2017) 14910–14914.
[38] L. Mandal, K.R. Yang, M.R. Motapothula, D. Ren, P. Lobaccaro, A. Patra, M. Sherburne, V.S. Batista, B.S. Yeo, J.W. Ager, J. Martin, T. Venkatesan, ACS Appl. Mater. Interfaces 10 (2018) 8574–8584.
[39] K.G. Schmitt, A.A. Gewirth, J. Phys. Chem. C 118 (2014) 17567–17576.
[40] K. Sun, C.Z. Wan, G.Z. Xu, Spectrochim. Acta Mol. Spectros 45 (1989) 1029–1032.
[41] H. Yang, Y.W. Hu, J.J. Chen, M. Balogun, P.P. Fang, S.Q. Zhang, J. Chen, Y. X. Tong, Adv. Energy Mater. 9 (2019) 1901396.
[42] Y.L. Deng, B.S. Yeo, ACS Catal. 7 (2017) 7873–7889.
[43] P. Liu, J.K. Nørskov, Phys. Chem. Chem. Phys. 2 (2001) 3814–3818.
[44] Y.J. Pang, J. Li, Z. Wang, C.S. Tan, P.L. Hsieh, T.T. Zhuang, Z.Q. Liang, C.Q. Zou, W. Wang, P.D. Luna, J.P. Edwads, Y. Xu, F.W. Li, C.T. Dinh, M. Zhong, Y.H. Lou, D. Wu, L.J. Chen, E.H. Sargent, D. Sinton, Nat. Catal. 2 (2019) 251–258.
[45] Q. Fan, M.L. Zhang, M.W. Jia, S.Z. Liu, J.S. Qiu, Z.Y. Sun, Mater. Today Energy 10 (2018) 280–301.

Wenjun Zhang received her B.S. degree in Chemistry from Anhui University, PR China (2015). She is now pursing her Ph.D. degree under the supervision of Prof. Zhong Jin in School of Chemistry and Chemical Engineering, Nanjing University, P.R. China. Her main interest is the design and fabrication nano-catalysts for electrochemical and photoelectrochemical reduction of carbon dioxide.

Chenhong Xu received her B.S.degree in Environment science from Nanjing University, PR China (2010). She was a visiting scholar under the supervision of Prof. Jin Ma in School of Chemistry and Chemical Engineering, Nanjing University, P.R. China (2018–2019). Her main interest is the theoretical design of electrocatalysts for reduction of carbon dioxide.

Yi Hu received his B.S. degree in Chemistry from Sichuan University in 2014. He is now pursuing his Ph.D. degree under the supervision of Prof. Zhong Jin in School of Chemistry and Chemical Engineering at Nanjing University. His research interests reside in two-dimensional nanomaterials for electrochemical energy storage and photoelectric conversion.

Songyuan Yang received his B.S. degree in Chemistry from Nanjing University in 2016. He is now pursing his Ph.D. degree under the supervision of Prof. Zhong Jin in School of Chemistry and Chemical Engineering, Nanjing University, P.R. China. His main interest is the design and fabrication nano-catalysts for electrochemical and photocatalytic reduction of carbon dioxide.

Lianbo Ma is now pursing his Ph.D. degree under the supervision of Prof. Zhong Jin in School of Chemistry and Chemical Engineering, Nanjing University, P.R. China. His main interest is the design and fabrication nanomaterials for energy storage and electrochemistry.

Lei Wang received his B.S. degree in Jiangsu University, PR China. He is now pursing his M.S. degree under the supervision of Prof. Zhong Jin in School of Chemistry and Chemical Engineering, Nanjing University, P.R. China. His main interest is the design of nano-catalysts for batteries.

Peiyang Zhao received his B.S. degree in Chemistry from Henan Polytechnic University, P.R. China (2015). He is now pursing his M.S. degree under the supervision of Prof. Zhong Jin at School of Chemistry and Chemical Engineering, Nanjing University. His main interest is the design and fa-brication of nanomaterials for perovskite solar cells and electrochemical energy storage.

Caixing Wang received his B.S. degree in Wuhan University, PR China. He is now pursing his Ph.D. degree under the supervision of Prof. Zhong Jin in School of Chemistry and Chemical Engineering, Nanjing University, P.R. China. His main interest is the design and fabrication of organic materials in flow batteries.

Prof. Jing Ma received her B.S and M.S. in Chemistry from Nanjing University of Science and Technology in 1992 and 1995, respectively, and a Ph.D. in Physical Chemistry from Nanjing University in 1998. She is currently a professor of chemistry at Nanjing University. She is primarily interested in developing electronic structure methods and molecular simulation methods and extending their applications to various functional material systems.

Prof. Zhong Jin received his B.S. (2003) and Ph.D. (2008) in chemistry from Peking University. He worked as a postdoctoral scholar at Rice University and Massachusetts Institute of Technology. Now he is a professor in School of Chemistry and Chemical Engineering at Nanjing University. He leads a research group working on functional nanomaterials and devices for energy conversion and storage.